# Atomistic simulations of copper oxidation and Cu/Cu$_2$O interfaces using charge-optimized many-body potentials

Bryce Devine,[1] Tzu-Ray Shan(單子睿),[1] Yu-Ting Cheng(鄭宇庭),[1] Alan J. H. McGaughey,[1,2] Minyoung Lee,[2]
Simon R. Phillpot,[1] and Susan B. Sinnott[1,*]

[1]*Department of Materials Science and Engineering, University of Florida, Gainesville, FL 32611-6400, USA*
[2]*Department of Mechanical Engineering, Carnegie-Mellon University, Pittsburgh, PA, 15213, USA*

Presented is a charge-optimized many-body potential (COMB) for metallic copper and copper oxide systems based on an extended Tersoff formalism coupled with variable charge electrostatics. To faithfully reproduce interactions between molecular oxygen and the metal surface, the potential includes atomic polarizabilities via both a point dipole model and dynamic partial charges, both of which are equilibrated through an extended Lagrangian scheme. The potential is fit to a training set composed of both experimental and *ab initio* computational data for cohesive energies, formation enthalpies, elastic properties, and surface energies of several metallic and oxide phases as well as bond dissociation energies for molecular oxygen and several of its anions. The potential is used in molecular dynamics simulations to model the Cu(111)‖Cu$_2$O(100) interface and the oxidation of the Cu (100) surface.

## I. INTRODUCTION

Historically, copper has been used as a model system for the fundamental study of early stage oxidation and oxide film growth of transition metal surfaces.[1–7] Notable studies of copper oxidation have been published over the past six decades since copper was included in the original work of Cabrera and Mott.[8] General findings that are consistent throughout a range of studies indicate that oxidation proceeds from chemisorption of atomic oxygen to the formation of an oxygen-deficient induction layer that facilitates the growth of three-dimensional Cu$_2$O islands.[6,9–11] While the current body of experimental work strongly supports a heteroepitaxial growth model in which rate is limited by oxygen surface diffusion,[6,10,12] the details of the metal and oxide morphology are somewhat contradictory in the literature. For instance, *in situ* transmission electron microscopy (TEM) experiments indicate a correlation between island nucleation and step edges.[3,13] However, a more recent study conducted at higher resolution found a more significant increase in growth rates at grain boundaries.[14,15] Diffraction and electron microscopy observations consistently indicate that Cu$_2$O islands form with the (110) plane of the oxide at the interface regardless of the structure of the metal surface upon which it forms.[2,3] Epitaxial growth oriented along the [110] direction of the metal is preferred.[2,3] While the termination of the oxide is invariant with the metal surface, the shape of the islands does vary among copper surfaces.[3] More recently, *in situ* TEM experiments indicate that island morphology also varies with reaction temperature.[12,15]

This leads to the promising possibility that if the mechanism of oxidation can be resolved to the point in which the dependence of island morphology on reaction conditions is understood at the atomic scale, controlled oxidation could be used as a means to direct the morphology of engineered oxide nanostructures. Resolving the oxidation mechanism requires a theoretical method with the fidelity and capability of efficiently modeling the structures of interest. One choice is an empirical potential that can be incorporated into a molecular dynamics (MD) or kinetic Monte Carlo scheme.

First-principles methods, such as density functional theory (DFT), have the highest fidelity currently available but are limited by both the size and the time scale of the problem. Because oxide formation is a diffusion-limited process that is influenced by strains at the interface,[6] atomic-scale simulation of the formation of a single small island involves tens of thousands of atoms, which exceeds the current capacity of traditional DFT methods by at least an order of magnitude. Hence, to enable the study of oxidation on a meaningful length scale, high-fidelity analytical interatomic potentials must be used.

In this work, we develop an interatomic potential suitable for modeling metallic Cu and Cu oxide phases and interfaces between Cu and Cu oxides, as well as for carrying out large-scale Cu oxidation simulations.

## II. METHODOLOGY

### A. Modeling Cu oxidation and Cu oxides

Copper forms pertinent oxides in two different oxidations states. Oxide islands and the initial oxide layer formed during oxidation of metallic copper are composed of cuprous oxide (Cu$_2$O), which is cubic with space group $Pn\bar{3}m$ [see Fig. 1(a)].[16] The structure can be viewed as a face-centered cubic (FCC) lattice of cations, with anions occupying $\frac{1}{4}$ of the tetrahedral sites at positions (1/4,1/4,1/4) and (3/4,3/4,3/4) or as a body-centered cubic (BCC) lattice of anions with cations occupying one half of the (1/4,1/4,1/4) positions. This results in twofold coordination around each cation with a linear O-Cu-O bond angle. As oxidation proceeds, the oxide phase converts to the monoclinic cupric oxide, CuO that has space group, $C2/c$ [see Fig. 1(b)].[17] The linear O-Cu-O bond persists in the higher oxide although the cation is now fourfold coordinated.

Simulations of oxide formation naturally fall under the scope of variable charge potentials that can simultaneously model the oxygen molecule, a metallic solid, and the evolving stoichiometry of the oxide as growth progresses. In choosing
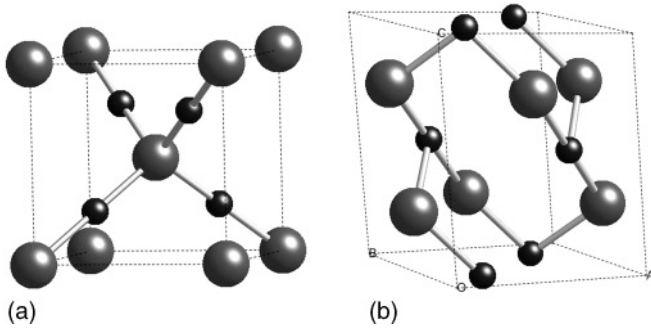
FIG. 1. Crystal structures for the two low-energy oxide phases of copper oxide. Large grey spheres represent O, and small black spheres are Cu. Cuprous oxide (a) forms a cubic lattice with $a = 4.27$ Å. Cupric oxide (b) forms a monoclinic crystal structure with $a = 4.68$ Å, $b = 3.42$ Å $c = 5.13$ Å, and $\beta = 99.6^\circ$.

a potential form for a metal-metal oxide system, a good first guess would be along the lines of an embedded atom method (EAM)[18] or second-moment-based potential such as Finnis-Sinclair[19] coupled with an electrostatic model. This approach was pursued by Streitz and Mintmire with their electrostatics+ (ES+) model for aluminum and alumina systems,[20] which coupled a variable charge electrostatic scheme to a Finnis-Sinclair bond-order potential. The ES+ model has subsequently been extended with some refinement to several additional oxide and alloy systems.[14,15]

However, the significant directionality in the bonding for the most relevant Cu oxide phases requires a potential optimized for covalent interactions, such as the Tersoff's potential.[21,22] Several recently published potentials link the variable charge (QEq) electrostatics with extended Tersoff-type potentials. For example, Yasukawa *et al.* developed one such potential for the covalent Si-SiO$_2$ system.[23] This potential was later refined by Yu *et al.* in their charge-optimized many-body (first-generation COMB) potential to reproduce the SiO$_2$ phase order[24] and by Shan *et al.* in their second-generation COMB potential for SiO$_2$ and amorphous silica.[25] The ReaxFF family of force fields employs a similar bond order dependent approach and has been adapted to several metal-oxide systems[26–28] and most recently Cu/Cu$_2$O/water interactions.[29] A significant concern with using a bond-order-based potential is its applicability to close-packed metals. However, as shown by Brenner, the functional form of Tersoff's bond-order potential is algebraically similar to the Finnis-Sinclair's potential with the addition of an angular dependence in the bond order term.[30] The applicability of this potential form to model metallic systems was demonstrated by Iwasaki *et al.*, who extended Yasukawa's potential to several metallic systems[31–33] and, more recently, by Yu *et al.*, who developed a modified form of Yasukawa's potential for metallic copper based on Iwasaki's parameterizations.[34] In this work, we start with the second-generation COMB potentials, and Yu's and Iwasaki's parameterizations provide a starting point from which to develop an analytical potential for the copper oxide phases.

### B. A dynamic charge electrostatic energy function

The electron density, $\rho(\mathbf{r})$, at each site, $i$, of a collection of ions exhibits a chemical potential, $\mu_i$, that has been shown

to be equivalent to the partial derivative of the energy, $U$, with respect to density: $\partial U / \partial \rho(\mathbf{r})$.[35] By this definition, $\mu_i$ is equivalent to the negative of the electronegativity, $\chi_i$ at each site. The principle of electronegativity equilibration (EE) states that in a closed system of interacting ions at chemical equilibrium, the electron density is distributed such that the electrochemical potential and hence the electronegativity is equal at all sites.[35] With the additional approximation that atomic charges occupy a fixed volume around each atom, $\mu_i$, can be defined as the partial derivative of energy with respect to partial charge: $\partial U / \partial q_i$, where $q_i$ is the partial charge of atom $i$. The partial charge on each atom can be determined as that which corresponds to the equilibrium electronegativity.

Determination of the equilibrium partial charges through the EE method requires an optimization of $N$ variables for each change in the atomic positions, where $N$ is the number of atoms in equilibrium. This is the most computationally burdensome portion of the method; Shan has shown that charge equilibration of COMB potentials usually takes as much as 80% of the computational time.[36] For efficiency and extensibility to larger system sizes, we use a simulated annealing technique. We make the charge and position of each atom dependent upon time and apply the Lagrangian introduced by Rick *et al.*[36]

$$L = \sum_{i=1}^{N} \frac{1}{2} m_i \dot{r}_i^2 + \sum_{i=1}^{N} \frac{1}{2} M_Q \dot{q}_i^2 - U\left[\{q\};\{\mathbf{r}\}\right] - \upsilon \sum_{i=1}^{N} q_i. \tag{1}$$

Here, $m_i$, $r_i$, and $q_i$ correspond to the mass, position, and charge of atom $i$, respectively. $M_Q$ is a fictitious charge mass. $\upsilon$ is an undetermined multiplier that enforces the constraint that charge in the system is conserved. The potential energy, $U[q,\mathbf{r}]$ is defined for a collection of ions, where q and $\mathbf{r}$ represent the set of atomic charges and positions. The evolution in time of the atomic positions and charges are given by the following equations of motion:

$$m_i \ddot{r}_i = \frac{\partial U[\{q\};\{\mathbf{r}\}]}{\partial r_i}. \tag{2}$$

$$M_Q \ddot{q}_i = \frac{\partial U[\{q\};\{\mathbf{r}\}]}{\partial q_i} - \upsilon_i. \tag{3}$$

$\upsilon$ is shown by Rick to be equal to the mean electronegativity and, when substituted in Eq. (3), gives

$$M_Q \ddot{q}_i = \chi_i - \bar{\chi}_i. \tag{4}$$

The partial charge on each atom is determined by iteratively solving the equations of motion with damping for each set of nuclear positions until the electronegativity, $\chi_i$, on each atom is sufficiently close to the mean electronegativity, $\bar{\chi}_i$, of the system. The tolerance, usually $10^{-3} - 10^{-5}$, used to determine whether the energy is minimized with respect to partial charges, is optimized to ensure energy conservation over the time span of the simulation. Compared to the traditional method of solving the charges via a self-consistent loop at each MD step, the Lagrangian method employed in this work does not involve taking the inverse of an $N$ by $N$ matrix. While the Lagrangian method includes a fictitious charge mass, charge time step, and an arbitrary damping factor,

it has better efficiency for scaling with $N$. The optimized charge mass and time step is $5.4858 \times 10^{-4}$ u and 0.0005 fs, respectively, and the damping is chosen to be 0.05.

The total potential energy function is composed of the electrostatic energy, $U^{es}$ and a short-range bond energy $U^{\text{bond}}$. The bond energy is composed of the pair sum over an analytical potential, $V^{\text{Bond}}(r_{ij})$, which will be described in the next section. The electrostatic energy for a systems of rigid atom-centered charge density distributions includes the energy to form a charge on each atom, $V^{\text{Self}}(q_i)$ and the Coulombic interaction between charges densities. For convenience, we make use of Streitz and Mintmire's rigid density distribution functions in which the density is a function of position, **r**, and charge:

$$\rho_i(\mathbf{r};q_i) = Z_i\delta(|\mathbf{r}-\mathbf{r}_i|) + (q_i - Z_i)f_i(|\mathbf{r}-\mathbf{r}_i|), \quad (5)$$

$$f(|\mathbf{r}-\mathbf{r}_i|) = \xi_i^3 \pi^{-1} \exp(-2\xi_i|\mathbf{r}-\mathbf{r}_i|). \quad (6)$$

Here, $Z_i$ is an effective point core charge treated as a fitted parameter. $\delta$ is the Kronecker delta function. $f(\mathbf{r})$ is a function that describes the radial decay of the charge density, where $\xi$ is an orbital exponent that controls the rate of decay. Integration over electron densities between pairs of atoms yields for the total electrostatic energy:

$$U^{es}[\{q\};\mathbf{r}] = \sum_i V_i^{\text{Self}}(q) + \frac{1}{2}\sum_i\sum_{j\neq i} q_i J_{ij}^{qq} q_j$$
$$+ \sum_i\sum_{j\neq i} q_i J_{ij}^{qz} Z_j. \quad (7)$$

$J^{qq}$ is the pairwise interaction between charge densities defined as the Coulomb integral:

$$J_{ij}^{qq} = [\rho_i|\rho_j] = \int d^3r_1 \int d^3r_2 \frac{\rho_i(\mathbf{r}_1)\rho_j(\mathbf{r}_2)}{r_{12}}, \quad (8)$$

where, $\mathbf{r}_1$ and $\mathbf{r}_2$ indicate the centers of $\rho_i(\mathbf{r})$ and $\rho_j(\mathbf{r})$. $r_{12}$ is the distance between density distributions. The charge-nuclear coupling operator, $J_{ij}^{qZ}$, in (7) is equal to a shielded nuclear attraction integral:

$$J_{ij}^{qZ} = [j|\rho_i] - [\rho_j|\rho_i], \quad (9)$$

$$[j|\rho_i] = \int d^3\mathbf{r} \frac{\rho_i(\mathbf{r})}{|\mathbf{r}-\mathbf{r}_i|}. \quad (10)$$

As indicated in (7), the interactions between point core charges are not explicitly determined but instead are assumed to be included in the bond energy, $V^{\text{Bond}}(r_{ij})$, along with all the non-electrostatic energy contributions.

For the self-energy, $V^{\text{Self}}$, we begin with the approach of Rappe and Goddard,[37] where the energy of a neutral atom as a function of charge may be expanded as a Taylor series:

$$V_i^{\text{Self}}(q_i) = E_i^0(0) + \chi_i q_i + J_{ii} q_i^2 + K_i q_i^3 + L_i q_i^4 + \cdots \quad (11)$$

$E^0(0)$ is the ground-state energy of a free atom. $\chi_i$ and $J_{ii}$ can be thought of as one of the centered integrals of the form $[i|\rho_i]$ and $[\rho_i|\rho_j]$, in which case they represent the self-interaction potential on each atom, $i$. The values for coefficients in Eq. (11) are treated as atom-specific parameters and are determined by

fitting to gas phase ionization potentials and electron affinities for each atom.

The pair interaction described by Eq. (8) includes an $r^{-1}$ term, which is solved via a direct Wolf summation[38] that is spherically truncated after 11 Å. This adds an additional function of $q^2$ to the self-energy, which is included implicitly in the fitted atomic coefficient, $J_{ii}$. In second-generation COMB potentials,[25,39] the self-energy contribution from the direct summation was considered extraneous from the potential. In those cases, when atoms interact, the contribution to the self-energy from the Wolf summation shifts the effective atomic ionization potential and electron affinities away from values of isolated atoms. By including all self-energy contributions in $V^{\text{self}}$, the atomic ionization energies are consistent between interacting and noninteracting atoms and are consistent with calculated reference values.

### C. The charge dependent bond order potential.

This work follows the Yasukawa formalism, where, with noncharged atoms, the short-range potential, $V^{\text{Bond}}(r_{ij})$, is equivalent to Tersoff's bond-order potential. The bond energy is described with a repulsive, $V^R$, and attractive, $V^A$, exponential functions of bond length, $r_{ij}$. The Yasukawa potential deviates from Tersoff in that the magnitude and radial decay of the pair interactions vary with charge. Charge-dependent correction functions, $D_i(q_i)$, are added to the exponential coefficient of the short-range energies to reflect the change in atomic radius with charge.

$$V^R(r_{ij},q_i,q_j) = F_c(r_{ij})A_{ij}$$
$$\times \exp\left\{-\lambda_{ij}r_{ij} + \tfrac{1}{2}[\lambda_i D_i(q_i) + \lambda_j D_j(q_j)]\right\}, \quad (12)$$

$$V^A(r_{ij}) = F_c(r_{ij})b_{ij}B_{ij}B_{ij}^*(q_i,q_j)$$
$$\times \exp\left\{-\alpha_{ij}r_{ij} + \tfrac{1}{2}[\alpha_i D_i(q_i) + \alpha_j D_j(q_j)]\right\}. \quad (13)$$

Here $A_{ij}$, $B_{ij}$, $\lambda_{ij}$, and $\alpha_{ij}$ are parameters that are determined for each bond type. The change in short-range contributions, $D_i(q_i)$, is specific to each element type. In particular,

$$D_i(q_i) = D_{U_i} + |b_{D_i}(Q_{U_i} - q_i)|^{n_{D_i}}, \quad (14)$$

$$b_{D_i} = (D_{L_i} - D_{U_i})^{\frac{1}{n_{D_i}}}/(Q_{U_i} - Q_{L_i}), \quad (15)$$

$$n_{D_i} = \frac{\ln D_{U_i} - \ln(D_{U_i} - D_{L_i})}{\ln Q_{U_i} - \ln(Q_{U_i} - Q_{L_i})}, \quad (16)$$

and $D_U$ and $D_L$ are parameters that reflect the change in atomic radius with charge. Likewise, $Q_U$ and $Q_L$ are the atomic charges that correspond to the limits of the valence shell.

Additionally, the bond energy is scaled with a charge-dependent function $B_{ij}^*(q_i,q_j)$ that reflects the change in bond order with charge:

$$B_{ij}^*(q_i,q_j) = (B_i^* B_j^*)^{\frac{1}{2}}, \quad (17)$$

$$B_i^* = [a_{B_i} - |b_{B_i}(q_i - Q_{O_i})|^{n_{B_i}}], \quad (18)$$

$$b_{B_i} = \frac{|a_{B_i}|^{\frac{1}{n_{B_i}}}}{\Delta Q_i}, \tag{19}$$

$$a_{B_i} = \left(1 - \left|\frac{Q_{O_i}}{\Delta Q_i}\right|^{n_{B_i}}\right)^{-1}, \tag{20}$$

$$\Delta Q_i = \tfrac{1}{2}\big(Q_{u_i} - Q_{L_i}\big), \tag{21}$$

$$Q_{O_i} = \tfrac{1}{2}\big(Q_{u_i} + Q_{L_i}\big). \tag{22}$$

$n_{B_i}$ is a fitted parameter. In Eq. (13), $b_{ij}$, is Tersoff's bond-order term that modifies the short-range attraction contribution based on bond angles, local symmetry, and number of nearest neighbors:

$$b_{ij} = \left[1 + \left(\beta_i \sum_{j\neq i}^{N} \sum_{k\neq i,j}^{N} \zeta_{ijk}(r_{ij}, r_{ik}) g(\theta_{ijk})\right)^{\eta_i}\right]^{\frac{-1}{2n_i}}, \tag{23}$$

$$\zeta_{ijk} = F_c(r_{ik}) \exp\left[a_{ij}^{m_i}(r_{ij} - r_{ik})^{m_i}\right], \tag{24}$$

$$g(\theta_{ijk}) = 1 + \frac{c_{ij}^2}{d_{ij}^2} - \frac{c_{ij}^2}{d_{ij}^2 + (h_{ij} - \cos\theta_{ijk})^2}. \tag{25}$$

$\alpha$, $\beta$, $\eta$, $m$, $c$, $d$, and $h$ are fitted parameters. The function, $F_c(r_{ij})$ smoothly terminates the short-range interactions within a cutoff region defined by two cutoff radii, $R_s$ and $S_s$:

$$F_C(r_{ij}) = \begin{cases} 1 & r_{ij} < R_{S-ij} \\ \frac{1}{2}\left[1 + \cos\left(\pi\frac{r_{ij}-R_{S-ij}}{S_{s-ij}-R_{S-ij}}\right)\right] & R_{S-ij} \leqslant r_{ij} \leqslant S_{S-ij} \\ 0 & r_{ij} > S_{S-ij} \end{cases} \tag{26}$$

### D. Charge independent short range energy functions

While the Yasukawa potential and the subsequent COMB formalism can be parameterized to provide a classical approximation of chemical bonding in the ideal ground-state structure, we have found it necessary to introduce additional interactions to reproduce the phase order of copper oxide and metallic copper phases, as well as to improve the behavior of molecular oxygen. A similar requirement was found necessary by Yu in the developing the first-generation COMB potential for SiO$_2$ and Cu.[24,34]

In the current potential, dependence of the bond energy on bond angle and coordination resides solely in the bond-order function that, in turn, gets smaller with increasing charge. This tends to be problematic for copper oxide phases, which exhibit directionality in the bonding in both the Cu(I) and Cu(II) oxides. In both cases, the O-Cu-O bond angle remains 180° with low coordination around Cu. The bond angle and coordination terms in $b_{ij}$ alone are insufficient to stabilize these structures. Therefore, additional charge-independent angular function based on the first-, second-, and third-order Legendre polynomials summed over the nearest neighbors (NN) is

included in the bond energy:

$$\begin{aligned} V_{ij}^{LP}(\cos\theta_{ijk}) = &\, K_{LP}^1 \left(1 + \sum_{j\neq i, k\neq i}^{NN} \cos\theta_{ijk}\right) \\ &+ K_{LP}^2 \left[1 + \frac{1}{2}\sum_{j\neq i, k\neq i}^{NN} (3.0\cos^2\theta_{ijk} - 1.0)\right] \\ &+ K_{LP}^3 \left[1 + \frac{1}{2}\sum_{j\neq i, k\neq i}^{NN} (5.0\cos^3\theta_{ijk} - 3.0\cos\theta_{ijk})\right]. \end{aligned} \tag{27}$$

$K_{LP}$ are fitted parameters specific to the bond type.

The potential overly stabilizes dense oxide phases such as CuO as rocksalt. An additional coordination-dependent term is needed to destabilize these higher coordination phases. The coordination correction first used in the ReaxFF force field[26,40] and later adapted by the COMB HfO$_2$ potential[39] is therefore also applied here:

$$V_i^{\text{Coord}}(\Delta N_i) = E_i^{\text{coord}}\Delta N_i \big/ \big(1 + \exp\left(\gamma_i^{\text{Coord}}\Delta N_i\right), \tag{28}$$

$$\Delta N_i = CN_i - CN_i^*, \tag{29}$$

$$CN_i = \sum_{j\neq i}^{NN} F_c(r_{ij}, R_{s-ij}, S_{s-ij}). \tag{30}$$

$CN^*$ is the coordination number of the element in the ideal structure, and $E^{\text{Coord}}$ and $\gamma_i^{\text{Coord}}$ are fitted parameters. The correction is only applied for Cu-O interactions such that $CN_i$ is the number of Cu-O bonds formed around atom $i$.

The charge-independent correction terms are consistent with the first-generation COMB potentials. Yu's potential for metals includes identical angular functions based on the Legendre polynomials to destabilize the HCP structure relative to FCC in close-packed metals. The coordination functions only apply to aberrant dense phases of the oxide and do not contribute to the ground-state energy of the oxide phases of primary interest in this work.

### E. Parameterization of the potential

The main goal of parameterization is to faithfully reproduce the surface and mechanical properties of the metal and the relative formation enthalpies of accessible oxide phases, while maintaining a reliable degree of transferability to possible nonstoichiometric oxides that may arise during oxidation. To ensure transferability, parameters are determined as a weighted least-squares best fit to a test set of properties of multiple phases with variation in coordination around the metal. The potential is further validated against an additional set of parameters such as surface energies, defect formation enthalpies, and mechanical properties determined with fully relaxed ionic positions.

This potential is an integral part of a family of COMB potentials, which are intended to be compatible with one another. However, in this work, we develop two slightly different parameterizations for the Cu/Cu$_2$O systems. The first set, labeled COMB2010, is based on the Cu potential Yu *et al.*,[24] is compatible with second-generation COMB potentials[25,39] and is optimized for interfacial and bulk structures. The second

set, labeled COMB2011, is designed to model bulk systems, small molecules, and single atoms in addition to interfaces. So as to provide maximum materials fidelity, a sacrifice to transferability is made in the second parameterization in that parameters for both atomic O and $O_2$ are different from those in the first- and second-generation COMB potentials.

To gain maximum flexibility in the parameterization, values are defined based on the interaction type. This is a deviation from the first-generation COMB potentials, where interaction parameters were determined from element-specific values via mixing rules.[24] However, in first-generation COMB potentials, correction functions that were specific to the interaction type were added to improve the potential performance. Since any gain in transferability is compromised with the correction terms, there is no perceived benefit in restricting the parameterization to atomic-based values. Furthermore, in practice, the mixing rules are found to be insufficient to describe critical interactions. For example, the angular coefficients for metals are very weak in the metallic phase. However, the oxide is characterized by a linear O-Cu-O bond that requires a stronger angular term than what is given by the mixing rules.

### 1. Parameterization of atomic and metallic copper

The electrostatic self-energy terms, $V^{\mathrm{Self}}$, for copper are determined as a least-squares best fit to the ionization potential and electron affinities determined at the coupled cluster level of theory using singlet and doublet and perturbative triplet excitations, CCSD(t).[41] A correlation consistent triple zeta basis set (cc-pVTZ)[42] is found to be sufficient to reproduce the first electron affinity and up to the third ionization potential. All *ab initio* calculations are performed with the Gaussian 03 computation suite.[43] When $V^{\mathrm{Self}}$ is truncated at the second order, the values may be derived directly from the first ionization potential and electron affinity provided that the energy of the neutral atom is taken as the zero point. However, we have found that higher-order terms are required to model energies beyond the first ionization potential, and is necessary for copper with two relevant oxidation states.

The starting point for charge-independent parameters are taken from Yu *et al.*,[34] which, in turn, are derived from the Iwasaki potential.[31] The cubic phase of $Cu_2O$ is basically an interpenetrating network that may be stabilized by covalent Cu-Cu bonding.[44,45] The Cu-Cu interaction in the oxide requires a longer cutoff than was used by Yu *et al.*, which, in turn, necessitates a refit of several parameters. The copper parameters at neutral charge are determined as the weighted least-squares best fit to experimental cohesive energy and lattice parameter of the FCC ground state. The training data set also includes unrelaxed values for the $C_{11}$, $C_{12}$, and $C_{44}$ elastic constants, (100), (110), and (111) surface energies and the vacancy formation energy, $E_F^V$. The energy vs volume for the FCC ground state as well as the relative energies of the BCC and natural hexagonal close-packed (HCP) structures are included in the training data set, as well.

Energy vs volume curves are calculated with DFT using the Vienna Ab Initio Simulation Package (VASP 4.6).[46] Energies are determined using the projector-augmented plane-wave method (PAW).[47] The PW91 generalized gradient approximation (GGA) is used for the exchange and correlation

energies. The kinetic energy cutoff is set at 400 eV. Integration over the Brillouin zone is performed over a $10 \times 10 \times 10$ Monkhorst-Pack $k$-point mesh.

The energy vs volume is calculated over a range of $\pm 5\%$ isometric strain and fit to the Rose equation of state.[48] The resulting equation of state captures the change in energy with volume in which the bulk modulus is constant at each strain point. For fitting purposes, the curves are generated with ionic positions fixed at ideal crystallographic positions, in which case the energy may not be a minimum and the forces may not be zero. The natural equation of state, generated with relaxed ionic positions, is used as a validation of the parameterization. The lattice parameters for higher energy phases that do not appear in the experimental phase diagram are not included in the training set: only their energies relative to the ground-state structure are considered. The atomic specific parameters for copper are tabulated in Table I, and interaction-dependent parameters are listed in Tables IIa and IIb. Table IIa lists parameters for COMB2010, and Table IIb lists parameters for COMB2011.

### 2. Parameterization of molecular oxygen

Oxygen parameters for the self-energy function, $V^{\mathrm{self}}$, are determined as a best fit to the ionization potential and to the first and second electron affinities of atomic oxygen calculated at the CCSD(t)/cc-pVTZ level of theory. The O-O interaction parameters are determined as a weighted least-squares best fit to energy vs bond length curves for $O_2$, $O_2^{1-}$, and $O_2^{2-}$ with the intent to capture the bond dissociation energy for the different charge states. Reference data for the energies vs bond length for the anions are also calculated using coupled cluster theory at the CCSD(t)/cc-pVTZ level. Lastly the polarizability tensor for $O_2$ and $O_2^{1-}$, determined via CCSD/cc-pVTZ, are also included in the training data set.

First- and second-generation COMB potentials for oxygen do not reproduce the dissociation behavior of the various anions of $O_2$, which is because $O_2$ anions were not included in the training set. The COMB2010 potential, for example, overstabilizes $O_2^{2-}$ to the point in which it is the most stable form of molecular oxygen. This is due to the $O^-$ anion being the lowest energy state of atomic oxygen and the rather large damping of Coulombic interactions at the $O_2$ bond distance. Our first-principles calculations predict $O_2^{2-}$ to be unstable at any bond length. In order to rectify this deficiency, the predicted dissociation behaviors of the $O_2$ anions of the COMB2011 potential are corrected with additional electrostatic functions. In particular the potential was expanded to include atomic polarizations via a point dipole model and a correction function that captures the effect of ionic neighbors on the atomic hardness coefficient.

The electronegativity equilibration principle has a well-defined basis in conceptual DFT, which seeks to explain chemical principles that govern reactivity in terms of DFT.[48] While pursuing fundamental definitions for such concepts as electronegativity and chemical hardness, that body of work suggests several improvements to consider in EE-based potentials. It has been shown that the self-Coulombic coefficient, $J_{ii}$, is equivalent to the atomic hardness.[49] Conceptual DFT

TABLE I. Atomic and electrostatic potential parameters.

| | COMB2010 | | COMB2011 | |
| --- | --- | --- | --- | --- |
| | Cu | O | Cu | O |
| $X$ (eV·q$^{-1}$) | 0 | 5.634414 | 3.768251 | 4.700782 |
| $J$ (eV·q$^{-2}$) | 4.321185 | 6.064346 | 2.966470 | 5.064537 |
| $K$ (eV·q$^{-3}$) | 0 | 4.514270 | 0.515044 | 2.756183 |
| $L$ (eV·q$^{-4}$) | 0 | 1.330079 | 0.257522 | 0.992188 |
| $\xi$ (Å$^{-1}$) | 0.454784 | 2.243072 | 1.476344 | 3.012029 |
| $Z$ (q) | 0 | 0 | 0.293153 | 0.030819 |
| $P$ (Å$^3$) | 0 | 0 | 0.335000 | 0.323757 |
| $P_1^J$ (eV·q$^{-3}$·r$^{-3}$) | $-0.274649$ | $-0.971086$ | $-0.470698$ | $-0.054039$ |
| $P_2^J$ (eV·q$^{-4}$·r$^{-5}$) | 0.725710 | $-3.922011$ | 1.086271 | 1.136518 |
| $D_u$ (Å) | $-0.161007$ | $-0.001120$ | $-0.307561$ | $-1.628749$ |
| $D_l$ (Å) | 0.167765 | 0.001480 | 0 | 0.244020 |
| $Q_u$ (q) | 2 | 5.504600 | 2 | 6 |
| $Q_l$ (q) | $-6$ | $-1.834900$ | $-6$ | $-2$ |
| $CN^*$ | 0 | 0 | 2.2 | 4.2 |
| $\gamma_{\text{Coord}}$ | 0 | 0 | 0.250000 | 0.249569 |
| $E_{\text{Coord}}$ (eV) | 0 | 0 | 0.597603 | 1.934556 |

suggests that the atomic hardness describes the Coulombic interaction when an atom is bound within a molecule or embedded in an ionic lattice.[49] In practice, EE methods are parameterized by either fitting the self-energy coefficients to atomic gas phase ionization potentials and electron affinities or by fitting to bulk properties. In the former case, the difference between bulk and atomic properties is compensated by other terms within the potential. In COMB2011, we fit to atomic values since we are interested in the interactions involving isolated atoms. To capture the change in atomic hardness as an atom is embedded in the bulk oxide, the hardness coefficient is augmented with a correction function that captures the change with its environment:

$$V_i^{\text{Self}}(r_i, q_i) = E_i^0(0) + \chi_i q_i + \left( J_i + \sum_{j \neq i}^{N} F_{ij}^{\text{Field}}(r_{ij}, q_j) \right) q_i^2$$
$$+ K_i q_i^3 + L_i q_i^4. \qquad (31)$$

Following the procedure outlined by Toufar *et al.*,[50] the environmental effect on the atomic hardness is determined by calculating the atomic self-energy at the CCSD(t)/aug-cc-PVTZ level in a symmetric field of point charges. The calculation is performed in a field of eight point charges arranged symmetrically around the atom at varying distance. The idea is to determine the effect of a confining potential on the atomic self-energy function. The sum of the charge on the point charges compensates the charge on the central atom such that the net charge of the system remains neutral, thus mimicking charge being transferred from the central atom to its neighbors. The Coulombic interaction between the point charges and the central atom and the interaction between point charges are subtracted from the total energy. Thus any change in the atomic self-energy function is due solely to the field effect of the point charges on the atomic self-energy. Figure 2 illustrates the calculated field effect of the lattice on the atomic self-energy of oxygen and copper. The effect is found to

TABLE II. (a) Bond-dependent potential parameters for COMB2010.

| | Cu-Cu | O-O | Cu-O | O-Cu |
| --- | --- | --- | --- | --- |
| A (eV) | 952.6931 | 3326.690 | 2966.036 | 2966.036 |
| B (eV) | 146.9871 | 260.8930 | 19.58262 | 19.58262 |
| $\lambda$ (Å$^{-1}$) | 2.794608 | 5.360000 | 4.475962 | 4.475962 |
| $\alpha$ (Å$^{-1}$) | 1.681711 | 2.680000 | 1.275175 | 1.275175 |
| $\beta$ | 0.140835 | 2 | 0.140835 | 2 |
| $\eta$ | 1 | 1 | 1 | 1 |
| m | 1 | 1 | 1 | 1 |
| c | 0 | 6.6 | 0 | 6.6 |
| d | 1 | 1 | 1 | 1 |
| h | 1 | $-0.229000$ | 1 | $-0.229000$ |
| $n_B$ | 10 | 10 | 10 | 10 |
| $R_s$ (Å) | 3.15 | 2.6 | 2.45 | 2.45 |
| $S_s$ (Å) | 3.35 | 3.0 | 2.65 | 2.65 |

TABLE II. (b) Bond-dependent potential parameters for COMB2011.

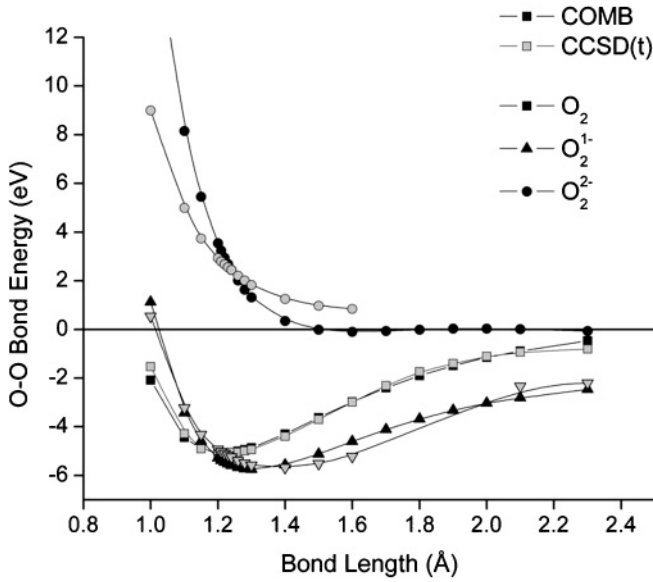| | Cu-Cu | O-O | Cu-O | O-Cu |
| --- | --- | --- | --- | --- |
| A (eV) | 712.3527 | 3523.359 | 598.29837 | 598.29837 |
| B (eV) | 102.8261 | 204.6259 | 102.5144 | 102.5144 |
| $\lambda$ (Å$^{-1}$) | 2.712035 | 5.516839 | 3.129308 | 3.129308 |
| $\alpha$ (Å$^{-1}$) | 1.467089 | 2.527568 | 1.433963 | 1.433963 |
| $\beta$ | 0.231055 | 2 | 0.231055 | 2 |
| $\eta$ | 1 | 1 | 1 | 1 |
| M | 1 | 1 | 1 | 1 |
| c | 0 | 43.56000 | 1.739680 | 2.043622 |
| d | 1 | 1 | 1 | 1 |
| h | 1 | $-0.22000$ | $-0.297973$ | 0.449820 |
| $n_B$ | 10 | 10 | 10 | 10 |
| $R_s$ (Å) | 3.2 | 2.2 | 3.2 | 3.2 |
| $S_s$ (Å) | 3.6 | 2.8 | 3.6 | 3.6 |

FIG. 2. The bond dissociation energy of $O_2$ anions: Black symbols are values from the potential fit. Grey symbols are calculated (CCSD(t)/cc-pVTZ).

decay with radial distance. A penalty function that captures the change in self-energy due to the field strength is fit to the results of the calculation:

$$F_i^{\text{Field}}(r_{ij}, q_j) = \frac{1}{4\pi\varepsilon_0} \sum_{j\neq i}^{NN} \left( \frac{P_1^J q_j}{r_{ij}^3} + \frac{P_2^J q_j^2}{r_{ij}^5} \right). \qquad (32)$$

$P_1^J$ and $P_2^J$ are fitted parameters. The starting point values for oxygen are determined as a least-squares best fit to the calculated ionization potential and first and second electron affinities determined in the various fields. These values are refined further along with the other electrostatic parameters to reproduce the dissociation behavior of $O_2$ such that the $O_2^{-1}$ anion is lower in energy than the ground state and $O_2^{-2}$ is unstable.

Molecular polarization represents a distortion in the electron density in response to an external electric field. The polarization response can be decomposed into atomic polarization, i.e., contributions due to the distortion of the electron density around each atom, change in the permanent dipole moment of the molecule due to variation in the overlap integrals between bonded atoms, and the exchange of charge between bonded atoms.[51] The dynamic charge scheme presented here uses nonpolarizable densities, meaning the charge distribution around the atom is fixed relative to the core. As a consequence the charge scheme mimics exchange charge polarization but does not reproduce atomic polarizations. The calculated polarizability tensor for molecular oxygen is anisotropic. The polarizability along the bond ($\sigma_\parallel$) of the molecule is composed of charge exchange and atomic polarizability and so registers a higher value [$\sigma_\parallel = 2.0$ Å$^3$ at the CCSD(t) level]. Polarizability perpendicular to the bond ($\sigma_\perp$) is only composed of atomic polarizabilities ($\sigma_\perp = 0.7$ Å$^3$). An EE-based dynamic charge scheme can only reproduce polarization parallel to the bond, so polarizabilities perpendicular to the bond are zero. The solution we employ here for the COMB2011 potential is to place a point dipole on

each atom similar to the fluctuating charge-fluctuating point dipole model by Sterne *et al.*[52]

With the fluctuating dipole model, the polarization vector is calculated directly from the electrostatic field generated by the atomic charges, $\vec{E}_i^q$, and the neighboring, induced dipoles.

$$\vec{\mu}_i = P_i \vec{E}(\vec{r}) = P_i \left[ \vec{E}_i^q + \sum_{j=1, j\neq i}^{N} T_{ij} \vec{\mu}_j \right], \qquad (33)$$

$$\vec{E}_i^q = \frac{1}{4\pi\varepsilon_0} \sum_{j\neq i}^{N} q_j \frac{\partial J_{ij}^{qq}}{\partial r} \frac{\vec{r}}{|\vec{r}_{ij}|}, \qquad (34)$$

where, $P_i$ is the polarizability tensor, and $T_{ij}$ is the dipole-dipole interaction tensor. For atoms with isotropic polarizabilities, as is the case here, $P$ reduces to a scalar value. Induced dipoles calculated in this manner suffer the same instability at close approach as the variable charges.[53] Consequently, $T_{ij}$ is employed as a damped function that diminishes as atoms overlap. For consistency, the same damping that is used with the Coulombic interactions is applied here:

$$T_{ij} = \frac{1}{4\pi\varepsilon_0 |\vec{r}_{ij}|^3} \left( 1 - 3\frac{\vec{r}_{ij} \cdot \vec{r}_{ij}}{|\vec{r}_{ij}|^2} \right)$$
$$\times \left[ 1 - e^{-2\xi_i r} \left( 1 + 2\xi_j r_{ij} + 2\xi_j^2 r_{ij}^2 \right) \right]. \qquad (35)$$

The additional energy contributions are the dipole self-energy, the dipole-charge interaction, and the dipole-dipole interactions:

$$U[\{q\}; \{\mathbf{r}\}] = \sum_i V_i^{\text{Self}}(q) + \frac{1}{2}\sum_i\sum_{j\neq i} q_i J_{ij}^{qq} q_j$$
$$+ \sum_i\sum_{j\neq i} q_i J_{ij}^{qz} Z_j + \frac{1}{2}\sum_i\sum_{j\neq i} V_{ij}^{\text{Bond}}(r_{ij})$$
$$+ \sum_i \frac{\vec{\mu}_i^2}{2\alpha_i} + \sum_i \vec{\mu}_i \cdot \vec{E}_i^q + \frac{1}{2}\sum_i\sum_{j\neq i} \vec{\mu}_i T_{ij} \vec{\mu}_j.$$
$$(36)$$

Atomic polarizabilities are fit to reproduce the polarizability of the $O_2$ dimer as well as the dissociation curve of the $O_2^-$ anion. The point dipole model affects the parameterization since a larger, induced dipole moment exists when charge is localized on one atom rather than distributed equally between atoms. As the bond is stretched, charge localizes on one atom, and the two atoms separate as atomic oxygen and an oxygen anion.

Figure 2 shows the CCSD(t) calculated and COMB2011 fit dissociation curve for several oxygen anions. It indicates that both the fit and calculated values predict $O_2^{1-}$ to be the most stable form of molecular oxygen at an extended bond length. Atomic parameters for oxygen are presented in Table I and O-O interaction parameters are listed in Tables IIa and IIb.

### 3. Parameterization of copper oxide

The energies for the oxide phases are fit to the enthalpy of formation, $\Delta H_f$, at 0 K rather than the cohesive energy. This allows for a comparison between phases of different stoichiometry and charge states. $\Delta H_f$ is determined as the total energy of the oxide phase minus the energy of the reactants in their reference states: $O_{2(g)}$ and $Cu_{(s)}$. Calculations

TABLE III. Coefficients for charge-independent bond angle energy functions.

|  | Cu-Cu | O-O | Cu-O-Cu | O-Cu-O |
|---|---|---|---|---|
| $K_{LP}^1$ (eV) | 0.073078 | 0.000000 | 0.069535 | 0.635646 |
| $K_{LP}^2$ (eV) | 0.000000 | 0.000000 | 0.000000 | 0.635646 |
| $K_{LP}^3$ (eV) | 0.019678 | 0.000000 | 0.100428 | 0.000000 |

are performed on ideal structures at 0 K for comparison to first-principles calculations where appropriate. The copper-oxygen interaction parameters and charge-dependent copper parameters are fit using a weighted least-squares best fit to $\Delta H_f$ of the cuprite phase of $Cu_2O$, CuO in the monoclinic ground state and high-pressure NaCl and CsCl phases, and the metastable paramelaconite phase of $Cu_4O_3$. The energy vs isometric strain and the unrelaxed elastic constants for $Cu_2O$ are also included in the fitting data set. Additionally, the training set includes the $\Delta H_f$ of a series of phases that are not manifested in the phase diagram; however, it is important to verify that the potential does not predict any of these to be more stable than the experimentally displayed phase. The additional structures examined have various coordination numbers on Cu: the antifluorite of $Cu_2O$ (4 on Cu) and $CuO_2$ as fluorite (8 on Cu), $\alpha$-cristobalite (4 on Cu), and $\beta$-cristobalite (4 on Cu).

As in the case of the metallic phase, formation enthalpies of the oxides are calculated using DFT with VASP 4.6. Energies are determined using the same functional energy cutoff and $k$-point mesh as were used for the metallic phase. The equilibrium lattice parameters for the ground state are scaled to experimental values for cuprous and cupric oxide. Energy vs isometric strain is determined relative to the scaled lattice constant. DFT typically underestimates the $\Delta H_f$ for copper oxides with reported values around $-1.24$ eV[54,55] compared to experimental values of $-1.75$ eV.[56] This is mainly due to the overbinding of the $O_2$ reference state in DFT. In this work, the energy of the $O_2$ molecule is fit to a higher level of theory than DFT, which reproduces the experimental bond enthalpy with greater accuracy. With the improved reference state energy for $O_2$, the fitted $\Delta H_f$ for $Cu_2O$ of 1.78 eV and deviates from experimental values by only 1.6%.

The difficulties with the $O_2$ reference state in DFT also apply to defect formation enthalpies, $\Delta H_f^{\text{def}}$.[57] Consequently, values for $\Delta H_f^{\text{def}}$ for point defects and surface energies that provide a reliable comparison to this potential are not available. $\Delta H_f^{\text{def}}$ for point and planar defects are thus used only for qualitative assessment of the final potential parameters. Finally, charge-dependent parameters are fit with the additional constraint that the electronegativity on each atom is $1.0 \times 10^{-6}$ eV/q in the ideal $Cu_2O$ structure. This ensures the ground state is a minimum in both real space and charge space. The full list of interaction parameters are tabulated in Tables IIa, IIb, and III.

## III. RESULTS AND DISCUSSION

### A. Properties of metallic copper

Properties of the metallic phase as predicted by the potential are compared in Table IV to experiment values, values calculated from first principles, results for Mishin's EAM

potential, Yu's previous Cu potential,[34,58] and the ReaxFF potential.[29] Elastic properties and surface energies are fit to values determined with fixed nuclear positions; however, the values listed in Table IV are determined with relaxed nuclear positions. The final parameter set reproduces the experimental elastic moduli and the $C_{11}$ and $C_{12}$ elastic constants. However, the $C_{44}$ elastic constant is about 30% lower than the calculated values. This weakness of the potential was also present in the earlier COMB parameterization.[34] The cohesive energies of the HCP, BCC, simple cubic, and diamond cubic phases are included in the training set. The values in Table IV are based on optimized structures using the final parameter set. The simple cubic and diamond cubic phases are fit with fairly low weight, which is reflected in the larger deviations from calculated values. However, the correct qualitative trends are maintained for these low coordination phases.

The formation enthalpies for common point defects and the stacking faults in the (111) plane are calculated as a validation of the potential. The results are listed in Table IV and compared to published reference values. The calculations for both planar and point defects are performed on a $36 \times 36 \times 36$ Å$^3$ supercell with periodic boundary conditions applied in three dimensions; the point defects are optimized at constant volume. The planar defect structures are allowed to relax their volume in the direction normal to the plane of the defect using a steepest descent algorithm. The energies are determined with dynamic charge equilibration. The point defect formation energy is determined relative to the reference state, which is defined as the total energy per atom in the perfect FCC lattice according to the following equation:[59]

$$E_F = n E_{\text{Def}} - (n \pm 1) E_{Cu}. \tag{37}$$

Here, $n$ is the number of atoms in the defect structure, $E_{\text{def}}$ is the energy per atom in the defect structure, and $E_{cu}$ is the energy per atom in the perfect FCC lattice. The predicted formation energies for Cu vacancies and the octahedral interstitial agree with experimental values[60] and other simulation methods. A calculation of the formation energies of the three dumbbell interstitials shows the 100 dumbbell to be the most energetically favorable, with a defect formation energy of 2.48 eV, in good agreement with experimental values.[60]

The relative energies for the (111), (100), and (110) surfaces agree with the values calculated from first principles[34] with a mean error of 3.8%. The surfaces take on a slight charge when relaxed with dynamic charge equilibration. The surface charge reflects the change in electron density due to the change in coordination at the surface. This is indicated in Fig. 3, which shows planes parallel to the (100) surface. As indicated in the figure, the (100) surface takes on a slight negative charge. The charge alternates between positive and negative with each subsequent plane down from the surface and returns to charge neutrality within seven lattice planes. The graph in Fig. 3 shows the variation in planar average charge density as determined by the potential. The charge returns to neutral about 10 Å from the surface. The values in parentheses in Table IV are determined with a charge of zero on each atom and no dynamic charge equilibration. The results are equivalent, indicating that the surface charge does not contribute significantly to the total surface energy for a pure metal.

TABLE IV. Properties of metallic copper.

| | Exp. | DFT[g] | EAM[f] | ReaxFF[h] | COMB2010 | COMB2011 |
|---|---|---|---|---|---|---|
| $a$ (Å) | 3.62[a] | 3.64 | 3.62 | 3.7 | 3.62 | 3.62 |
| $E_0$ (eV/atom) | −3.54[b] | −3.50 | −3.54 | −3.49 | −3.54 | −3.54 |
| *Bulk Modulus* (GPa) | 139[c] | 140 | 140 | | 139 | 139 |
| $C_{11}$ (GPa) | 170[c] | 173 | 173 | | 170 | 171 |
| $C_{12}$ (GPa) | 123[c] | 123 | 123 | | 123 | 123 |
| $C_{44}$ (GPa) | 75.8[c] | 80.1 | 76.2 | | 49 | 47.7 |
| $\alpha$ ($10^{-6} K^{-1}$) | 16.5[b] | | | | 14.5 | 16.9 |
| $\Delta E_o$ Phase transitions (eV/atom) | | | | | | |
| HCP | | 0.006 | 0.008 | | 0.008 | 0.008 |
| BCC | | 0.038 | 0.046 | 0.065 | 0.017 | 0.014 |
| Cubic | | 0.47 | 0.43 | 0.598 | 0.49 | 0.38 |
| Diamond | | 1.04 | 1.08 | 0.882 | 0.94 | 0.99 |
| $\Delta H_f$ Point defects (eV) | | | | | | |
| $V_{Cu}$ | 1.28[d] | | 1.27 | | 1.21 | 1.17 |
| $Cu_i - oct$ | 2.8 − 4.2[e] | | 3.06 | | 2.41 | 4.93 |
| *$Cu_i$ 100 dumbell | 2.8 − 4.2 | | | | | 2.48 |
| *$Cu_i$ 110 dumbell | 2.8 − 4.2 | | | | | 6.91 |
| *$Cu_i$ 111 dumbell | 2.8 − 4.2 | | | | | 8.58 |
| Planar defects (mJ·m$^{-2}$) | | | | | | |
| $\gamma_{(100)}$ | 1780[f] | 1478 | 1345 | | 1599 | 1478(1478)** |
| $\gamma_{(110)}$ | 1780 | 1609 | 1475 | | 1646 | 1519(1519) |
| $\gamma_{(111)}$ | 1780 | 1294 | 1239 | | 1295 | 1218(1218) |
| $\gamma_{ISF}$ | 61[g] | 34.3 | 36.2 | | 44.4 | 46.3(46.3) |
| $\gamma_{USF}$ | 162 | 210 | 161 | | 224 | 105(105) |
| $\gamma_{Twin}$ | 24[g] | 19.2 | 18.2 | | 45 | 23.2(23.2) |

*Indicates predicted values. All other values are included in the training set.
**Values in parentheses are determined with charge equilibration.
[a]Reference 56.
[b]Reference 82.
[c]Reference 83.
[d]Reference 84.
[e]Reference 60.
[f]Reference 85.
[g]Reference 86.
[h]Reference 29.

Calculated formation enthalpies for the stacking faults reflect trends predicted by the other reference methods. As shown in Table IV, the potential predicts a higher formation
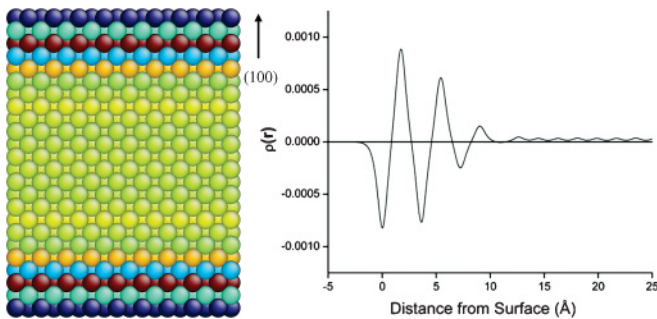


FIG. 3. (Color online) Surface charge in metallic copper. The copper surface exhibits a negative charge. The charge normal to the (100) plane is shown. Color corresponds to charge with blue = −0.1 and red −0.1 charge units. The plot shows the planar charge density distribution normal to the (100) surface.

energy for the intrinsic stacking fault than the COMB2010 parameterization. Examining the COMB2011 potential, the predicted formation energy is closer to experimental values but differs from DFT values[34] by a greater degree. The predicted extrinsic stacking fault energy is improved over the COMB2010 potential; however, the unstable stacking fault energy is underestimated by the COMB2011 parameter set relative to all other referenced methods. The reason for the underestimation of stacking fault energies is directly influenced by the Legendre polynomial bond angle correction terms. A careful fine-tuning of the polynomial parameters in subsequent versions of the potential can improve its performance in applications in which improved mechanical properties of the metal are required. Here, however, the angular corrections for the metal are tuned to optimize properties of the metal and the oxide phases, rather than the metal alone.

As with surfaces, the unstable stacking fault and point defect energies take on a slight charge, reflecting the change in coordination. The results of the calculations performed without variable charges are listed in parentheses alongside the charge optimized values in Table IV. The fact that the

TABLE V. Ionization potentials (IP) and electron affinities (EA) in electron volts for Cu and O.

| Cu | *Ab initio* | COMB2010 | COMB2011 |
|---|---|---|---|
| First *EA* | 1.08 | 4.32 | 1.08 |
| First *IP* | 7.43 | 4.32 | 7.43 |
| Second *IP* | 20.3 | 17.28 | 18.6 |
| O | | | |
| First *EA* | 1.40 | 2.75 | 1.40 |
| Second *EA* | −6.08 | 1.84 | −6.08 |
| First *IP* | 13.5 | 17.54 | 13.5 |

TABLE VI. Properties of molecular oxygen.

| | *Ab initio* | COMB2010 | COMB2011 |
|---|---|---|---|
| Bond length (Å) | 1.21[a] | 1.20 | 1.21 |
| Bond energy (eV) | −5.17[a] | −5.11 | −5.17 |
| Polarizability of $O_2$ (Å$^3$)[b] | | | |
| $\alpha^{11}$ | 2.0 | – | 2.2 |
| $\alpha^{22}$ | 0.69 | – | 0.65 |
| $\alpha^{33}$ | 0.69 | – | 0.65 |

[a]Reference 56.
[b]ccsd(t)/cc-pvTZ.

results are the same indicates that the effect of charge on pure metal planar defects is very slight. The differences between this parameterization of the COMB2011 potential and that of Yu *et al.*[34] are, therefore, attributable to the refitting of the parameters rather than the inclusion of electrostatic interaction.

### B. Properties of molecular oxygen

The self-energy functions for both elements are determined as the least-squares best fit to calculated values for electron affinities and ionization potentials. The success of the COMB2011 fit is reflected in the values listed in Table V. The COMB2011 potential is able to capture the dissociation behavior of oxygen and its anions as illustrated in Fig. 2. COMB reproduces the lowest energy state of $O_2$ at longer bond lengths to be the $O_2^-$ anion with a charge of −0.5 on each atom, which is consistent with higher-level calculations that predict the lowest energy charge state to be $O_2^-$. The $O_2^{2-}$ anion from COMB2011 is unstable until it dissociates into separate $O^-$ anions. This agrees well with *ab initio* methods up to CCSD(t)/aug-cc-pVTZ level of theory.

The polarizability of oxygen is fit along with the other electrostatic parameters. The starting point for the fit is the atomic polarizability calculated to be 0.716 Å$^3$ using CCSD(t)/cc-pVTZ. The fitted value of 0.36 Å$^3$ underestimates the atomic values but successfully reproduces the components of the polarizability tensor of the $O_2$ molecule as shown in Table VI.

### C. Properties of copper oxide

The lattice parameter, formation enthalpy, unrelaxed bulk modulus, shear modulus, and the $C_{11}$, $C_{12}$, and $C_{44}$ elastic constants for $Cu_2O$ are included in the training data set. The results in Table VII are for relaxed atomic positions. The $C_{44}$ elastic constant exhibits a large drop due to ionic relaxation and consequently exhibits a larger deviation from the reference values. The COMB2011 parameterization shows significant improvement over the COMB2010 parameterization and reproduces the properties from first-principles calculations.

For the oxide phases, defect formation enthalpies $\Delta H_f^{\text{def}}$ must consider the chemical potential of species added or removed from the system.[54]

$$\Delta H_F^{\text{Def}} = E_{\text{Def}} - E_0^{\text{0Bulk}} \pm \sum_i n_i \mu_i. \tag{38}$$

Here, $\mu_i$ is the chemical potential of species $i$ and $n_i$ is the number of atoms of species $i$ added or removed from the

perfect structure to form the defect. $E_{\text{Def}}$ is the energy of the defect structure, and $E_0^{\text{Bulk}}$ is the energy of the perfect structure. $\mu_i$ depends on the conditions under which the defect is formed such that $\mu_i = \mu^* - \Delta\mu$, where $\mu^*$ is the chemical potential of the reference state.[54] For $Cu_2O$ to form, the relationship $2\mu_{Cu} + \mu_O = \mu_{Cu2O}$ must be true. Furthermore, if we neglect the small dependence on pressure of $\mu_{Cu2O}$, then $2\mu_{Cu} + \mu_O = \Delta H_{f-Cu2O}$. In the copper-rich (oxygen-lean) limit, where $Cu_2O$ is in equilibrium with metallic Cu, $\mu_{Cu}$ is equal to the chemical potential of metallic Cu, $\mu_{Cu(s)}$, which in COMB is taken as the total energy per atom in the perfect FCC lattice. In contrast, the oxygen-rich limit, $\mu_{Cu}$ is zero and $\mu_O = \Delta H_{f-Cu2O}$.[54,55,61]

For comparison, values for $\Delta H_f^{\text{def}}$ are determined at the copper-rich limit for several point defects; the results are listed in Table VII. The relative energies for the oxygen defects, $V_o$ and $O_i$, from COMB2011 agree qualitatively with the results of first-principles calculations[54,55,61]; however, a large discrepancy is shown for $V_O$ described by COMB2010. In addition, the formation enthalpies for $V_{Cu}$ from both COMB potentials are higher than the experimental reference values. However, here and in the DFT reference values, the $\Delta H_f^{\text{def}}$ is determined for the charge neutral defect, meaning $V_{Cu}$ is formed by removing a neutral Cu atom from the ideal crystal. This is unlikely in real systems in which an ion is more likely to be removed. A lower energy charged defect most likely accounts for the discrepancy between the experimental and computational results. $\Delta H_f^{\text{def}}$ for Cu interstitials from COMB2010 are slightly negative, which is mainly due to the strong covalent attraction between cations. $\Delta H_f^{\text{def}}$ for other defects agree qualitatively with the DFT values considering that $\mu_O$ varies by 0.51 eV between DFT and COMB.[55]

In a manner similar to point defect calculations, the surface energies of the oxide consider the chemical potential of the species added or removed from the perfect crystal to form the surface.[55]

$$\gamma = \frac{1}{A} \left( G \pm \sum_i n_i, \mu_i \right). \tag{39}$$

Here, $A$ is the surface area and $\gamma$ is the surface-free energy. In the COMB potential, the calculations are performed at 0 K, where contributions due to entropy are zero, allowing direct comparison with reported DFT values. $\mu_{Cu}$ and $\mu_O$ at the oxygen-lean limit are used for comparison to reported values under similar conditions.[55] The (111) surface is the only stoichiometric surface listed in Table VII. This surface also

TABLE VII. Properties of $Cu_2O$ (cuprous oxide).

| | Experiment | First principles | ReaxFF[h] | COMB2010 | COMB2011 |
|---|---|---|---|---|---|
| $a$ (Å) | 4.27[a] | 4.31[e] | 4.24 | 4.25 | 4.27 |
| $E_{coh}$ (eV/$Cu_2O$) | 11.3[b] | 11.4[e] | | 11.9 | 11.4 |
| $\Delta H_F$ (eV) | −1.73[b] | −1.24[e] | −1.96 | −2.33 | −1.75 |
| *Bulk Modulus* (GPa) | 112[c] | 112 | | 94 | 111 |
| *Shear Modulus* (GPa) | | 8.15 | | 46 | 8.27 |
| $C_{11}$ (GPa) | 123[c] | 123 | | 105 | 122 |
| $C_{12}$ (GPa) | 108[c] | 107 | | 89 | 105 |
| $C_{44}$ (GPa) | 12[c] | 12.1 | | 71 | 57.3 |
| Cu charge | | | | 0.79 | 0.54 |
| Point defects in $Cu_2O$ (eV)[g] | | | | | |
| $V_{Cu}$ | 0.45[d] | 0.28–1.17[e] | | 1.34 | 2.49 |
| $V_{Cu_{split}}$ | 0.25[d] | 0.78–1.24[e] | | | 2.20 |
| $V_O$ | | 1.55[e] | | 5.68 | 0.95 |
| $O_{i_{tet}}$ | | 1.36–1.47[e] | | 1.74 | 0.71 |
| $O_{i_{Oct}}$ | | 1.69–1.9[e] | | 2.95 | 2.26 |
| $Cu_{i_{tet}}$ | | 1.47[e] | | −0.18 | 0.95 |
| $Cu_{i_{Oct}}$ | | 1.9[e] | | −0.17 | 0.97 |
| Surface energies (mJ·m$^{-2}$)[g] | | | | | |
| $Cu_2O$(100):Cu | | 1570[f] | | 3483 | 1510 |
| $Cu_2O$(100):O | | 1070[f] | | 1490 | 1030 |
| $Cu_2O$(110):Cu | | 1790[f] | | 2428 | 2380 |
| $Cu_2O$(110):CuO | | 417[f] | | 951 | 603 |
| $Cu_2O$(111) | | 785[f] | | 1425 | 783 |

[a]Reference 16.
[b]Reference 56.
[c]Reference 87 and 88.
[d]Reference 89.
[e]Reference 54, 55 and 61.
[f]Reference 90.
[g]Defect formation and surface energies correspond to oxygen lean conditions.
[h]Reference 29.

gives the best agreement between methods. A general trend of the surface energies is exactly reproduced: oxygen-terminated surfaces have lower surface energies than copper-terminated ones. It is also found that the CuO terminated (110) surface is the most stable surface of $Cu_2O$.

Since $Cu_2O$ is not the only possible oxide form of Cu, the properties of monoclinic CuO are also considered in the fitting scheme. The modeling of CuO is complicated by the symmetry-breaking Jahn-Teller distortion that characterizes structures containing d$^9$ transition metals.[62] The effect cannot be modeled with current DFT implementations.[57] Classical potentials have had better success in replicating the effect where the $Cu^{2+}$ cation is modeled as an aspherical ion with a distorted neighbor shell.[62] This special feature of the $Cu^{2+}$ cation has also been shown an affect the Jahn-Teller distortion of $[Cu(OH_2)_6]^{2+}$ molecules.[29] The COMB formalism has two means of replicating asymmetry in the neighbor shell: the Legendre polynomial angle correction and the point dipole model. In this work, only the CuO heat of formation, rather than the structural properties (particularly the lattice parameters) is fit explicitly; however, the lattice parameters were utilized to check if the parameter set reasonably predicts the CuO structure. Table VIII indicates that the COMB2011 potential predicts the properties of this phase with reasonably good fidelity. Although the lattice parameters deviate from the

low-temperature values[34], the total volume of the structure is comparable to DFT results as shown in Fig. 4. Polarization does not improve the results, as indicated in the last column in Table VIII.

Table IX lists $\Delta H_f$ for several oxide phases from experiments, first-principles calculations, the ReaxFF potential and the COMB2011 potential. The experimental $\Delta H_f$ for $Cu_4O_3$ is lower in energy than $Cu_2O$, indicating that $Cu_2O$ is only stable under oxygen-lean conditions.[63] As shown in Table IX, the relative formation enthalpies for the three low-energy oxide phases as predicted by the COMB2011 potential are consistent with experimental values. This is further illustrated in Fig. 4, which plots the energy per unit volume for the three low-energy

TABLE VIII. Properties of monoclinic CuO.

| | Experimental | COMB | COMB + polar |
|---|---|---|---|
| a (Å) | 4.68[a] | 4.36 | 4.33 |
| b (Å) | 3.42[a] | 3.74 | 3.77 |
| c (Å) | 5.13[a] | 5.04 | 5.05 |
| $\beta$ (Deg.) | 99.6[a] | 97.1 | 97.1 |
| $\Delta H_F$ (eV) | −1.63[b] | −1.68 | −1.68 |

[a]Reference 17.
[b]Reference 56.

TABLE IX. $\Delta H_f$ (in eV) of copper oxides.

|  | Structure | Experimental | DFT/simulation | ReaxFF[e] | COMB |
|---|---|---|---|---|---|
| $Cu_2O$ | Cuprite | −1.73[a] | −1.24[b] | −1.96 | −1.75 |
| CuO | Tenorite | −1.63[c] | −1.11[b] | −1.91 | −1.63 |
| $Cu_4O_3$ | Paramelaconite | −4.72[c] | −5.74[c] |  | −5.11 |
| CuO | CsCl |  | −0.53[d] |  | −0.31 |
| CuO | NaCl |  | −1.24[d] | −1.05 | −1.22 |
| $CuO_2$ | $\alpha$-Cristobalite |  | −0.30[d] |  | −1.58 |
| $CuO_2$ | $\beta$-Cristobalite |  | −0.34[d] |  | −1.31 |
| $CuO_2$ | Fluorite |  | −1.29[d] |  | −0.49 |
| $Cu_2O$ | Antifluorite |  | −1.14[d] |  | −0.44 |

[a]Reference 56.
[b]Reference 54.
[c]Reference 63.
[d]This work.
[e]Reference 29.

phases. In Fig. 4 the volume and energy vs isometric strain for the CuO and $Cu_2O$ structures compare well with values from DFT.

It should be noted that the ReaxFF potential for Cu/$Cu_2$O/$H_2$O[29] yields very reasonable properties, which are very comparable to that from COMB2011 for both Cu and $Cu_2$O as presented in Tables IV and IX. This is not surprising since there are significant overlaps between the training databases of the ReaxFF and COMB potentials. It is reasonable to expect that this ReaxFF potential also produces reliable properties for the Cu and $Cu_2$O interfaces, as well as the Cu oxidation processes. A comparison of the Cu surface oxidation process and oxide growth with both ReaxFF and COMB potentials is reserved for future studies.

### D. Behavior of $O_2$ on the Cu surface

#### 1. Molecular oxygen adsorption on the Cu (100) surface

The behavior of $O_2$ on the Cu (100) surface as predicted by COMB2011 is used as a test of the potential. The enthalpy of adsorption, $\Delta H_{\rm Ads}$, and dissociative adsorption of $O_2$ on the Cu (100) surface is determined by placing $O_2$ at several sites and minimizing the energy of the structure via a steepest descent algorithm. $\Delta H_{\rm Ads}$ is determined using an equation similar to Eq. (40):

$$\Delta H^{\rm Ads} = E_{Cu-O_2}^{(100)} - E_{Cu_{(s)}}^{(100)} - \mu_{O_2}. \qquad (40)$$

$E_{Cu_{(s)}}^{(100)}$ is the energy of the Cu substrate with a free (100) surface. $\Delta H_{\rm Ads}$ is determined under oxygen-rich conditions, where $\mu_O = 1/2\ {\rm E}_{O_{2(g)}}$.[54]
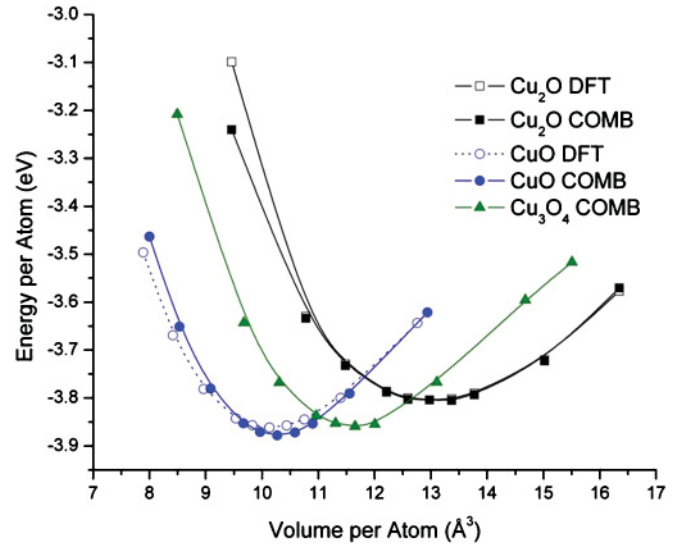


FIG. 4. (Color online) The energy per unit volume of the three low-energy phases of copper oxide. Filled symbols represent COMB-predicted values. Open symbols represent DFT values.

The images to the left in Figs. 5(a)–5(f) show the initial sites selected for study. The results are compared with values calculated via DFT in Table X. When the initial position of the $O_2$ molecule is 2 Å above the metal surface, the molecule relaxes to a local minimum that is 2.18 Å above the surface with a $\Delta H_{\rm Ads}$ of −2.51 eV. The molecule does not dissociate at this point, and only a small charge of −0.092 is transferred to the molecule. When the $O_2$ is placed 1.8 Å above the surface, the molecule relaxes toward the surface and dissociates at atop

TABLE X. $\Delta H_{\rm Ads}$ (in electron volts) and height (in angstroms) of $O_2$ on Cu (100) surface.

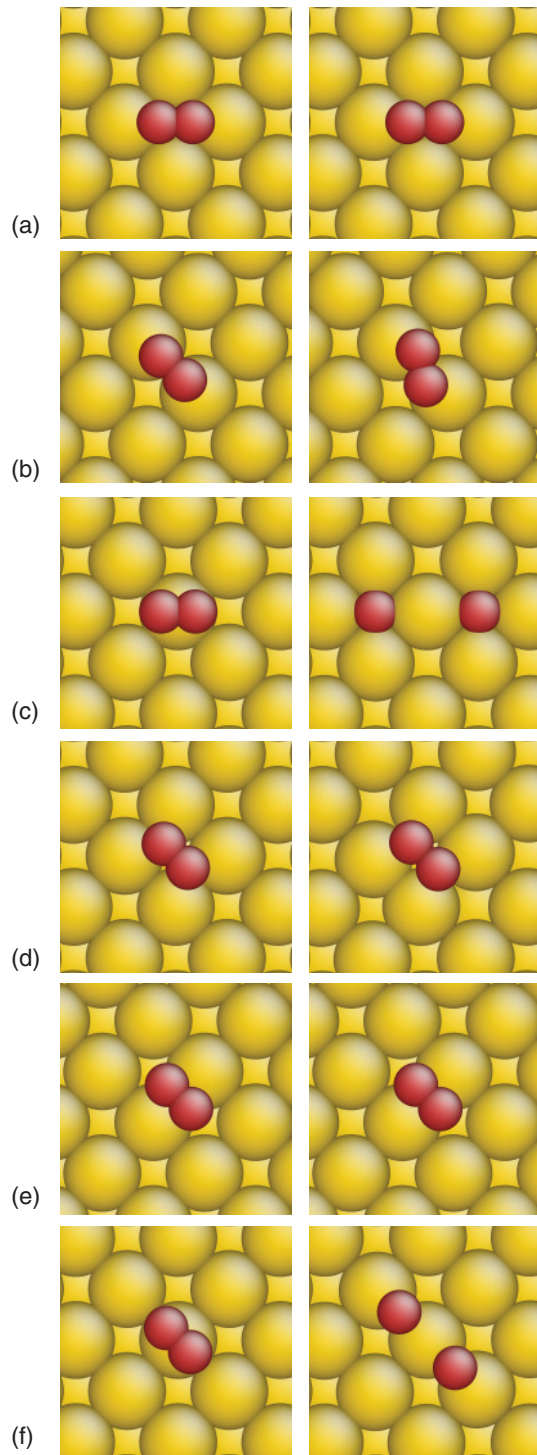|  | Hollow 1 | Bridge 1 | Atop 1 | Hollow 2 | Bridge 2 | Atop 2 |
|---|---|---|---|---|---|---|
| $\Delta H_{\rm Ads}$ (DFT) | −2.0 | −2.2 | −2.2 | −2.9 | −4.0 | −2.4 |
| $\Delta H_{\rm Ads}$ (COMB) | −0.1 | −1.4 | −3.4 | −0.9 | −0.1 | −1.4 |
| Height (COMB) | 2.3 | 1.9 | 0.7 | 1.4 | 2.2 | 1.4 |
| $\Delta H_{\rm Bar}$ (COMB) | 0.7 | 1.0 | 0.1 | 0.3 | 5.0 | 0.1 |

FIG. 5. (Color online) $O_2$ is placed on the Cu (100) surface in six orientations (a) Hollow site 1, (b) Bridge site 1, (c) Atop site 1, (d) Hollow site 2, (e) Bridge site 2, and (f) Atop site 2 relaxed, using the COMB potential. The initial and final geometries are shown to the left and right, respectively. The small red spheres represent O, and the large yellow ones are Cu. Initial orientations are 1.8 Å above the metal surface; final heights are given in Table X.

sites but not at bridge and hollow sites. The relaxed positions are shown to the left of Figs. 5(a)–5(f). The energies in Table X indicate that the lowest $\Delta H_{Ads}$ occurs when an $O_2$ molecule
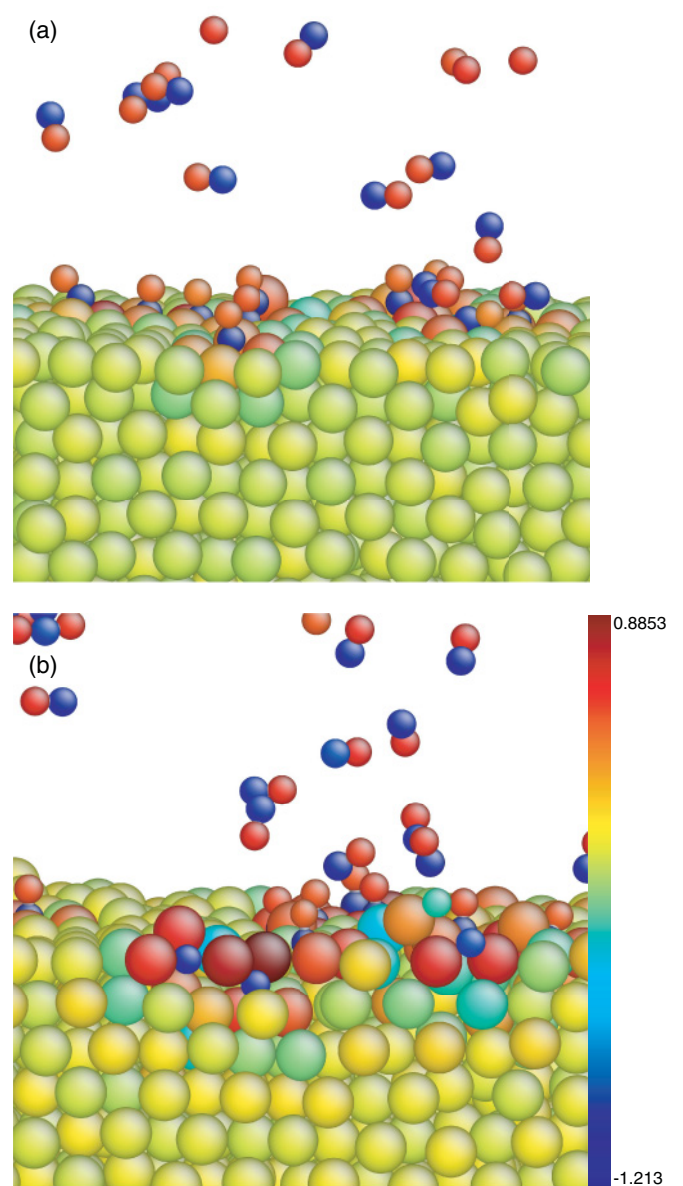


FIG. 6. (Color online) Oxygen molecules on clean Cu (100) surface at 1000 K, (a) after 1 ps and (b) after 3 ps. Larger spheres are Cu, and smaller ones are O. The color corresponds to charge with red $=0.89e$ and blue $= -1.21e$.

is positioned at an atop site and relaxes to a state where the O atoms are dissociated and absorbed into neighboring fourfold hollow sites. This corresponds to the configuration shown in Fig. 5(c), and the label Atop 1 in Table X. The third row in Table X lists the final height of the oxygens on the Cu surface, and Atop 1 site also exhibits the lowest height since O atoms are adsorbed on to the hollow sites. We have also investigated the values of $\Delta H_{Ads}$ determined with the point dipole contribution turned off, whereas the overall effect is only $\sim$0.1 eV. COMB values for $\Delta H_{Ads}$ are compared to values determined via first-principles calculations. In particular COMB and DFT give the same relative trends, both predicting dissociation to the hollow sites as being most energetically favorable.

The last row in Table X lists the energy barrier, $\Delta H_{Bar}$, for $O_2$ to dissociate on each site calculated from COMB;

it indicates that $O_2$ dissociation reactions on these sites are endothermic. The energy barriers for the atop sites, $\sim$0.1 eV, are the lowest compared to other sites; consistent with the dissociation behaviors. Additionally, the dissociation energy barrier for the Hollow 2 site from the COMB-predicted energy barrier value is 0.3 eV; although 2.3 times larger than our first-principles DFT calculations (0.13 eV), considering this is a pure prediction, instead of a fitted property, COMB2011 potential is reasonably predicting the dissociation of $O_2$ on Cu (100) surface.

### 2. Oxidation of Cu (100) surfaces

Copper oxide is a promising nanostructure for microelectronic devices because of its diverse morphologies of $Cu_2O$ islands with difference temperatures. Therefore, oxygen coverage on the Cu (100) surface and the resulting reconstructions have been the subject of numerous theoretical and experimental studies.[64–73] With the STM technique, different reconstructed Cu (100) surfaces, which depend on oxygen coverage, are observed.[72,73] At oxygen coverage less than 0.3 monolayers (ML), the surface is characterized by microdomains formed in a c($2 \times 2$) arrangement, which can be described as oxygen atoms occupying the fourfold hollow sites. When the oxygen coverage rises above 0.5 ML, the missing-row $2\sqrt{2} \times \sqrt{2}R45°$ reconstructed surface will be induced.[72,73] To study the interaction between oxygen molecules and the Cu surfaces with MD simulations, oxygen molecules are placed on Cu (100) surface, roughly 3 Å–5 Å. The oxygen partial pressure is estimated to be around 100 oxygen atoms. The surface structure is composed of clean Cu (100) without oxygen at the subsurface and the missing-row reconstructed surface. This structure was then annealed for 10 ps at 1000 K. Figure 6(a) illustrates the interaction between oxygen molecules and the clean Cu (100) surface. It indicates that 30% of the oxygen molecules are adsorbed with positively charged oxygen atoms pointing toward the hollow sites of the Cu surface. The first dissociation of an oxygen molecule on the clean Cu (100) surface was observed after 2 ps, and second one was observed sequentially at the frame of 2.7 ps. Fig. 6(b) indicates that the dissociated oxygen atoms with negative charge are located at the hollow sites of the surface.

In contrast to the clean Cu (100) surface, dissociated oxygen atoms have not been observed on the top of the missing-row reconstructured surface for 10 ps. It has been reported that the oxygen-induced reconstructed Cu (100) surface is repulsive to oxygen molecules,[74] which implies that the subsurface oxygen atoms may induce a strong barrier for further dissociation of oxygen molecules. Therefore, higher surface temperatures or longtime scaled methods are needed to investigate this aspect of the oxidation process. In summary, the COMB2011 potential demonstrates that oxygen is molecularly adsorbed on the clean Cu (100) surface and migrates until sites with a lower dissociation barrier are found. The potential indicates that the dissociations take place when the oxygen molecules move close to the hollow site of Cu (100) surface. To further investigate the transition from missing-row reconstructed surface to $Cu_2O$ islands, which involves longer time-scaled simulations, we are currently implementing the COMB po-
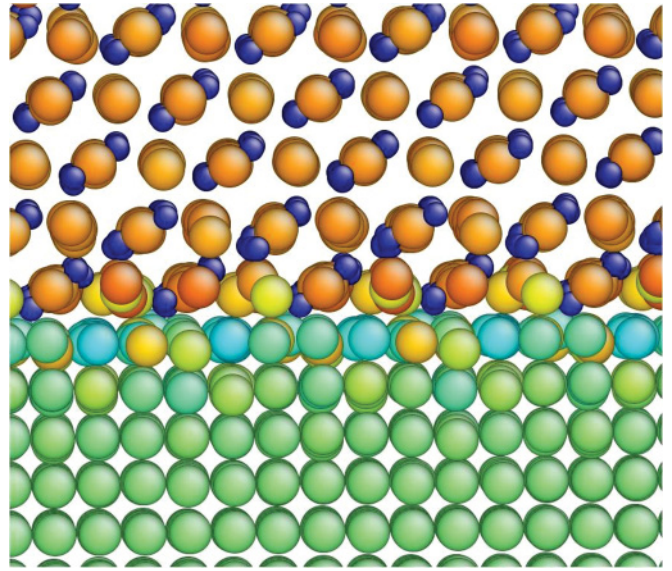


FIG. 7. (Color online) The $Cu_2O(111)\|Cu$ (100) interface viewed along the Cu[100] direction after annealing at 200 K for 10 ps. Color corresponds to charge with red $= -1.3$ e and blue $= 1.3$ e. The larger spheres are Cu. The smaller spheres are O. The interfacial region where the lattices are disrupted is confined to the first Cu layer in the oxide and one to two layers in the metal.

tentials within the adaptive kinetic Monte Carlo (AKMC) method.[75]

### E. Simulations of the $Cu_2O(111)\|Cu$ (100) interface

The metal oxide interface is not well characterized in the literature. This is partly due to the graded nature of
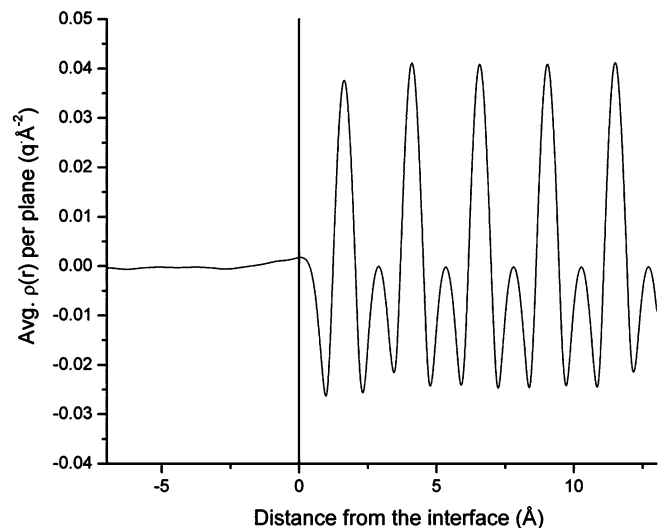


FIG. 8. Planar average charge density across $Cu_2O(111)\|$ Cu (100) interface after annealing at 200 K for 10 ps. Values are calculated per atom, giving the average charge density per atom in each plane parallel to the interface. The zero point in the graph corresponds to the original interface. The oxide phase is on the positive side of the zero point. There is a slight charge transfer between phases at the interface, which is limited to the first two planes in each phase. Charge varies slightly around zero in the metal.

most of the interfaces, which form from an oxygen-induced reconstructed surface. One means of obtaining an atomically sharp interface is through the electrochemical deposition of $Cu_2O$.[76] When deposited on the Cu (100) surface, $Cu_2O$ forms a film with initial growth in the [111] direction.[76] The resulting $Cu_2O(111)\|Cu$ (100) interface is atomically sharp and suspected to be semicoherent, although this exact structure has not been confirmed experimentally. As a final check of the potential, a model of the interface is relaxed and annealed at 50, 100, 200, 300, and 450 K using the COMB2011 potential. The model consists of a $35.3 \times 31.4 \times 36.2$ $Å^3$ supercell containing a 20-Å-thick slab of $Cu_{(s)}$ interfaced with a 15.3-Å-thick slab of $Cu_2O$. Periodic boundary conditions are applied in three dimensions; in other words, no vacuum space exists between the slabs, so the periodic image is one of alternating metal and oxide slabs stacked upon one another.

The epitaxial relationship between the metal and oxide is $Cu_2O(111)[11\bar{2}]\|Cu$ (100)[001], which gives a lattice mismatch of 3.64% along the epitaxial direction. The slab is annealed under constant temperature and pressure (NPT) for 10 ps at each temperature. An MD timestep of 0.1 fs is used. The temperature is maintained via a Nosé-Hoover thermostat.[77–79] The system cell is fixed in three dimensions; during relaxation, the symmetry of the supercell is constrained to remain orthorhombic. After relaxation the adhesion energy of the interface is estimated to be 2.77 $J/m^2$, compared to 2.10 $J/m^2$ from our first-principles calculations.

The interface is predicted to be stable at all the temperatures considered. The first interfacial layers in both phases rearrange beginning at 100 K, suggesting either a lower-energy epitaxial relationship or reconstruction exist. Figure 7 shows the interface after annealing for 10 ps at 300 K, viewed along the Cu [100] or $Cu_2O[11\bar{2}]$ direction. During the simulation there is no evidence of a phase transformation beyond the first layer or atomic diffusion between phases, suggesting the potential is predicting the correct ground-state configuration. There is also only a negligible charge transfer between phases, as indicated in Fig. 8, which indicates the planar average charge density with distance from the interface. The figure indicates that charge transfer is limited to the interfacial region of one Cu layer in the oxide and one to two layers in the metal. The charge leaking across the $Cu/Cu_2O$ interface is negligible, which is a result of the field effect (Eq. (32)). However in the original charge model employed by the first-generation COMB potential for $SiO_2$,[24] the charge leaking across the $Si/SiO_2$ interface is significant, which leads to unphysical negatively charged first-layer Si atoms in the Si substrate

(Fig. 9 of Ref. 24). This deficiency is rectified with the improved charge model presented in this work.

Considering the computational efficiency of the COMB2011 potential presented in this work, the charge equilibration step is the most time-consuming part in the calculations. A benchmark test of the COMB potential implemented in the Large-scale Atomic/Molecular Massively Parallel Simulator[80] (LAMMPS) software showed that when compared to the Lennard-Jones potential, COMB potential takes approximately ~280 factors more computational time. Compared to Tersoff[22], AIREBO,[81] and ReaxFF[40] potentials implemented in the same software, COMB potential is approximately 70.0, 5.0, and 1.5 times slower, respectively.

## IV. CONCLUSIONS

Based on results from the simulations and calculations, a reactive potential composed of a short-range bond order potential coupled with variable charge electrostatics is shown to be capable of simulating the ground-state bonding environments of Cu as both a pure metal and when oxidized to $Cu_2O$. The potential also captures the bonding behavior of oxygen as a pure element interacting with $Cu_{(s)}$ and when incorporated in the $Cu_2O$ oxide. This enables the large-scale simulation of processes such as oxidation of the metal surface or phenomena across the metal oxide interface.

The potential successfully reproduces a monoclinic unit cell for the higher oxide CuO with the correct volume and formation enthalpy but noticeable deviated lattice parameters. Since the relative energy for the phases are consistent with experimental values, the potential is useful for studies of the initial stages of oxidation up until the formation of CuO. Future work should seek to improve the potential in this regard. Lastly, the simulations performed in the course of this work are only intended to demonstrate the stability and capabilities of the potential formalism. A more thorough examination of the materials and processes simulated here are left for future work.

## ACKNOWLEDGMENTS

*ssinn@mse.ufl.edu

[1]L. O. Brockway and I. M. Adler, J. Electrochem. Soc. **119**, 899 (1972).

[2]K. Heinemann, D. B. Rao, and D. L. Douglass, Oxid. Met. **9**, 379 (1975).

[3]R. H. Milne and A. Howie, Philos. Mag. A **49**, 665 (1984).

[4]A. Ronnquist and H. Fischmeister, J. Inst. Met. **89**, 65 (1960).

[5]F. W. Young, J. V. Cathcart, and A. T. Gwathmey, Acta Metall. **4**, 145 (1956).

[6]G. A. Kaminski, H. A. Stern, B. J. Berne, R. A. Friesner, Y. X. X. Cao, R. B. Murphy, R. H. Zhou, and T. A. Halgren, J. Comput. Chem. **23**, 1515 (2002).

[7]J. C. Yang, M. Yeadon, B. Kolasa, and J. M. Gibson, Microsc. Microanal. **4**, 334 (1998).

[8]N. Cabrera and N. F. Mott, Rep. Prog. Phys. **12**, 163 (1948).

[9]K. Tanaka, T. Inomata, and M. Kogoma, Thin Solid Films **386**, 217 (2001).

[10]J. C. Yang, D. Evan, and L. Tropia, Appl. Phys. Lett. **81**, 241 (2002).

[11]J. C. Yang, B. Kolasa, J. M. Gibson, and M. Yeadon, Appl. Phys. Lett. **73**, 2841 (1998).

[12]L. Sun and J. C. Yang, J. Mater. Res. **20**, 1910 (2005).

[13]R. H. Milne, Surf. Sci. **232**, 17 (1990).

[14]R. Drautz, D. A. Murdick, D. Nguyen-Manh, X. W. Zhou, H. N. G. Wadley, and D. G. Pettifor, Phys. Rev. B **72**, 144105 (2005).

[15]D. G. Pettifor, M. W. Finnis, D. Nguyen-Manh, D. A. Murdick, X. W. Zhou, and H. N. G. Wadley, Mater. Sci. Eng. A Struct. Mater. **365**, 2 (2004).

[16]R. W. G. Wyckoff, *Crystal Structures* (John Wiley & Sons, New York, 1963).

[17]N. E. Brese, M. Okeeffe, B. L. Ramakrishna, and R. B. Vondreele, J. Solid State Chem. **89**, 184 (1990).

[18]M. S. Daw and M. I. Baskes, Phys. Rev. B **29**, 6443 (1984).

[19]M. W. Finnis and J. E. Sinclair, Philos. Mag. A **50**, 45 (1984).

[20]F. H. Streitz and J. W. Mintmire, Phys. Rev. B **50**, 11996 (1994).

[21]J. Tersoff, Phys. Rev. B **37**, 6991 (1988).

[22]J. Tersoff, Phys. Rev. B **38**, 9902 (1988).

[23]A. Yasukawa, JSME Int. J., Ser. **39**, 313 (1996).

[24]J. G. Yu, S. B. Sinnott, and S. R. Phillpot, Phys. Rev. B **75**, 085311 (2007).

[25]T.-R. Shan, B. D. Devine, J. M. Hawkins, A. Asthagiri, S. R. Phillpot, and S. B. Sinnott, Phys. Rev. B **82**, 235302 (2010).

[26]K. Chenoweth, A. C. T. van Duin, P. Persson, M. J. Cheng, J. Oxgaard, and W. A. Goddard, J. Phys. Chem. C Nanomater. Interfaces **112**, 14645 (2008).

[27]D. Raymand, A. C. T. van Duin, M. Baudin, and K. Hermansson, Surf. Sci. **602**, 1020 (2008).

[28]Q. Zhang, T. Cagin, A. van Duin, W. A. Goddard, Y. Qi, and L. G. Hector, Phys. Rev. B **69**, 045423 (2004).

[29]A. C. T. van Duin, V. S. Bryantsev, M. S. Diallo, W. A. Goddard, O. Rahaman, D. J. Doren, D. Raymand, and K. Hermansson, J. Phys. Chem. A **114**, 9507 (2010).

[30]D. W. Brenner, Phys. Status Solidi B **217**, 23 (2000).

[31]T. Iwasaki and H. Miura, J. Mater. Res. **16**, 1789 (2001).

[32]T. Iwasaki, J. Mater. Res. **19**, 1197 (2004).

[33]T. Iwasaki, J. Mater. Res. **20**, 1300 (2005).

[34]J. Yu, S. B. Sinnott, and S. R. Phillpot, Philos. Mag. Lett. **89**, 136 (2009).

[35]R. G. Parr, R. A. Donnelly, M. Levy, and W. E. Palke, J. Chem. Phys. **68**, 3801 (1978).

[36]T.-R. Shan, Doctoral dissertation, University of Florida, 2011.

[37]A. K. Rappe and W. A. Goddard, J. Phys. Chem. **95**, 3358 (1991).

[38]D. Wolf, P. Keblinski, S. R. Phillpot, and J. Eggebrecht, J. Chem. Phys. **110**, 8254 (1999).

[39]T.-R. Shan, B. D. Devine, T. W. Kemper, S. B. Sinnott, and S. R. Phillpot, Phys. Rev. B **81**, 125328 (2010).

[40]A. C. T. van Duin, S. Dasgupta, F. Lorant, and W. A. Goddard, J. Phys. Chem. A **105**, 9396 (2001).

[41]G. D. Purvis and R. J. Bartlett, J. Chem. Phys. **76**, 1910 (1982).

[42]T. H. Dunning, J. Chem. Phys. **90**, 1007 (1989).

[43]M. J. Frisch, H. B. Schlegel, and G. E. Scuseria, Gaussian 03 (Gaussian Inc., Wallingford CT, 2004).

[44]E. Ruiz, S. Alvarez, P. Alemany, and R. A. Evarestov, Phys. Rev. B **56**, 7189 (1997).

[45]K. Takahashi, A. Itoh, T. Nakamura, and K. Tachibana, Thin Solid Films **374**, 303 (2000).

[46]G. Kresse and J. Hafner, Phys. Rev. B **47**, 558 (1993).

[47]P. E. Blochl, Phys. Rev. B **50**, 17953 (1994).

[48]J. H. Rose, J. R. Smith, F. Guinea, and J. Ferrante, Phys. Rev. B **29**, 2963 (1984).

[49]P. Geerlings, F. De Proft, and W. Langenaeker, Chem. Rev. **103**, 1793 (2003).

[50]H. Toufar, K. Nulens, G. O. A. Janssens, W. J. Mortier, R. A. Schoonheydt, F. DeProft, and P. Geerlings, J. Phys. Chem. **100**, 15383 (1996).

[51]B. G. Dick and A. W. Overhauser, Phys. Rev. **112**, 90 (1958).

[52]H. A. Stern, G. A. Kaminski, J. L. Banks, R. H. Zhou, B. J. Berne, and R. A. Friesner, J. Phys. Chem. B **103**, 4730 (1999).

[53]B. T. Thole, Chem. Phys. **59**, 341 (1981).

[54]H. Raebiger, S. Lany, and A. Zunger, Phys. Rev. B **76**, 045209 (2007).

[55]A. Soon, X. Y. Cui, B. Delley, S. H. Wei, and C. Stampfl, Phys. Rev. B **79**, 035205 (2009).

[56]D. R. Lide, *CRC Handbook of Chemistry and Physics* (CRC Press, Boca Raton, FL, 2005), p. D-41.

[57]D. O. Scanlon, B. J. Morgan, and G. W. Watson, J. Chem. Phys. **131** (2009).

[58]Y. Mishin, D. Farkas, M. J. Mehl, and D. A. Papaconstantopoulos, Phys. Rev. B **59**, 3393 (1999).

[59]M. Finnis, *Interatomic Forces in Condensed Matter* (Oxford University Press, Oxford, 2003), p. 155.

[60]M. Sprik, J. Phys. Chem. **95**, 2283 (1991).

[61]M. Nolan, Thin Solid Films **516**, 8130 (2008).

[62]S. M. Woodley, P. D. Battle, C. R. A. Catlow, and J. D. Gale, J. Phys. Chem. B **105**, 6824 (2001).

[63]K. J. Blobaum, D. Van Heerden, A. J. Wagner, D. H. Fairbrother, and T. P. Weihs, J. Mater. Res. **18**, 1535 (2003).

[64]M. J. Harrison, D. P. Woodruff, J. Robinson, D. Sander, W. Pan, and J. Kirschner, Phys. Rev. B **74**, 165402 (2006).

[65]H. Iddir, D. D. Fong, P. Zapol, P. H. Fuoss, L. A. Curtiss, G. W. Zhou, and J. A. Eastman, Phys. Rev. B **76**, 241404 (2007).

[66]K. W. Jacobsen and J. K. Norskov, Phys. Rev. Lett. **65**, 1788 (1990).

[67]F. Jensen, F. Besenbacher, E. Laegsgaard, and I. Stensgaard, Phys. Rev. B **42**, 9206 (1990).

[68]T. Kangas, K. Laasonen, A. Puisto, H. Pitkanen, and M. Alatalo, Surf. Sci. **584**, 62 (2005).

[69]I. Merrick, J. E. Inglesfield, and H. Ishida, Surf. Sci. **551**, 158 (2004).

[70]I. K. Robinson, E. Vlieg, and S. Ferrer, Phys. Rev. B **42**, 6954 (1990).

[71]S. Stolbov, A. Kara, and T. S. Rahman, Phys. Rev. B **66**, 245405 (2002).

[72]K. Lahtonen, M. Lampimaki, M. Hirsimaki, and M. Valden, J. Chem. Phys. **129**, 194707 (2008).

[73]K. Lahtonen, M. Hirsimaki, M. Lampimaki, and M. Valden, J. Chem. Phys. **129**, 124703 (2008).

[74]M. Alatalo, A. Puisto, H. Pitkänen, A. S. Foster, and K. Laasinen, Surf. Sci. **600**, 1574 (2006).

[75]G. Henkelman and H. Jónsson, J. Chem. Phys. **111**, 7010 (1999).

[76]J. K. Barton, A. A. Vertegel, E. W. Bohannan, and J. A. Switzer, Chem. Mater. **13**, 952 (2001).

[77]W. G. Hoover, Phys. Rev. A **31**, 1695 (1985).

[78]S. Nose, J. Chem. Phys. **81**, 511 (1984).

[79]S. Nose, Mol. Phys. **52**, 255 (1984).

[80]S. J. Plimpton, J. Comput. Phys. **117**, 1 (1995).

[81]S. J. Stuart, A. B. Tutein, and J. A. Harrison, J. Chem. Phys. **112**, 6472 (2000).

[82]S. A. Adelman and J. D. Doll, J. Chem. Phys. **64**, 2375 (1976).

[83]G. Simons and H. Wang, *Single Crystal Elastic Constants and Calculated Aggregate Properties* (MIT Press, Cambridge, 1977).

[84]R. W. Balluffi and A. P. Sutton, *Intergranular and Interphase Boundaries in Materials*, edited by A. C. Ferro, J. P. Conde, and M. A. Fortes, Part 1, Materials Science Forum, Vol. 207 (Trans Tech Publications, Switzerland, 1996), pp. 1–12.

[85]Y. Mishin, M. J. Mehl, D. A. Papaconstantopoulos, A. F. Voter, and J. D. Kress, Phys. Rev. B **63**, 224106 (2001).

[86]M. B. J. Wijesundara, Y. Ji, B. Ni, S. B. Sinnott, and L. Hanley, J. Appl. Phys. **88**, 5004 (2000).

[87]M. M. Beg and S. M. Shapiro, Phys. Rev. B **13**, 1728 (1976).

[88]J. Hallberg and R. C. Hanson, Phys. Status Solidi **42**, 305 (1970).

[89]W. Pauli, Z. Phys. **31**, 765 (1925).

[90]A. Soon, M. Todorova, B. Delley, and C. Stampfl, Phys. Rev. B **75**, 125420 (2007).